Size effects in microstructured superconductors and quantum materials

Fermin, R.

Citation

Fermin, R. (2022, December 7). *Size effects in microstructured superconductors and quantum materials*. *Casimir PhD Series*. Retrieved from https://hdl.handle.net/1887/3492762

Version:	Publisher's Version
License:	Licence agreement concerning inclusion of doctoral thesis in the Institutional Repository of the University of Leiden
Downloaded from:	https://hdl.handle.net/1887/3492762

Note: To cite this publication please use the final published version (if applicable).

7

CONTROLLING CHIRAL DOMAIN WALLS IN MESOSCOPIC Sr_2RuO_4 USING GEOMETRY AND IN-PLANE MAGNETIC FIELDS

I would like to acknowledge contributions from: G. Stam, J. Ridderbos, A. Brinkman, J. Aarts, K. Lahabi & Y. Maeno

Despite more than a quarter-century of tremendous experimental and theoretical effort, the pairing symmetry of the correlated electron superconductor Sr_2RuO_4 remains elusive. Regardless of the pairing symmetry, however, some of these works found evidence of superconducting chiral domains in bulk crystals. In previous research, we were able to trap a single chiral domain wall, separating such domains, in mesoscopic rings of Sr_2RuO_4. In this chapter, we further examine the properties of these domain walls and find that they are stable over a large range of sample geometries that are either singly or doubly connected. By obtaining the Shapiro response of our samples, we provide definite proof of the Josephson coupling of the domain-wall-associated junctions and gain insight into the periodicity of their current-phase relation. We show that we can alter the domain structure by applying small in-plane magnetic fields (in the ab-plane; $H < H_{c1}$), which manifests itself as the appearance of half-integer Shapiro steps in the IV-characteristic. Furthermore, we find that the in-plane fields can unpin the chiral domain walls, which results in a bistability of the critical current. By applying either a positive or negative current bias, we switch between a low and high I_c state, which resembles a superconducting memory element. Combined, the experiments in this chapter form compelling evidence for the presence of chiral domains, which, in light of recent literature, indicates that a chiral d-wave order parameter describes superconductivity of Sr_2RuO_4.

To be submitted.

7.1. INTRODUCTION

The pairing symmetry of a superconductor determines many of its characteristics and is often established soon after its discovery. The famous example is d-wave superconductivity in the high T_c cuprates[1–3], which was experimentally established within eight years after its Nobel-prize-winning discovery in 1986[4]. Despite plentiful experimental and theoretical efforts, the pairing symmetry of the unconventional superconductor Sr_2RuO_4 has remained one of the larger open questions of condensed matter physics for over the last quarter-century. At the time of writing, there are two main classes of proposals: an order parameter characterized by a two-component nature, with $d_{xz} \pm i d_{yz}$ as the most prominent candidate, or an accidental degeneracy between two single-component order parameters, where $s \pm i d_{xy}$ and $d_{x^2-y^2} \pm i g_{xy(x^2-y^2)}$ are most promising.

A possible way of discriminating between the two classes is the proposed chirality of the order parameter. In a chiral superconductor, the superconducting ground state is two-fold degenerate, which leads to the spontaneous emergence of superconducting domains, each corresponding to a single chirality. Therefore, detecting these domains provides direct evidence for a chiral pairing symmetry. $p_x \pm i p_y$ and $d_{xz} \pm i d_{yz}$ are such chiral pairing symmetries, for example, while p_x and $d_{x^2+y^2}$ are not. Instead of detecting the domains, we can also focus on the chiral domain walls separating them. At the domain wall, the order parameter of both chiralities is locally suppressed, which manifests itself as a Josephson junction[5]. Since the domain size is typically in the micrometer range, trapping a single domain wall in experiments is impossible in macroscopic crystals. This provides a strong motivation for reducing the size of the crystals in well-controlled geometries.

In previous work, we found the emergence of spontaneous Josephson junctions in mesoscopic rings of Sr_2RuO_4, which we interpreted as chiral domain walls associated with a chiral p-wave pairing symmetry[6]. In this chapter, we provide further examination of these domain walls. By obtaining measurements of Shapiro steps on these junctions, we not only provide definitive proof of the Josephson coupling but also a further study of the periodicity of the current-phase relation of the domain wall junctions. We find that, under the application of small in-plane fields, the periodicity of the current-phase relation can be altered, which leads to the observation of fractional Shapiro steps. Furthermore, in-plane fields reveal a two-level state in the critical current of the junctions, where the application of electrical current can be used to switch between each state, resembling a superconducting memory. Finally, we will try to provide a reinterpretation of these results based on the most recent experimental and theoretical works considering the pairing symmetry of Sr_2RuO_4. To achieve this goal, this chapter will commence with a history of the experimental progress on the pairing symmetry in Sr_2RuO_4.

7.2. BRIEF EXPERIMENTAL HISTORY OF THE PAIRING SYMMETRY IN Sr_2RuO_4

Soon after its discovery of in 1994[7], it was noted that superconductivity in Sr_2RuO_4 is highly sensitive to non-magnetic disorder and that it bears many similarities to the A-phase of liquid ^{3}He[8–10]. This started the search for experiments and theoretical models that further examine the pairing symmetry[11, 12]. This section will give a brief overview of these experiments.

7.2.1. AN UNCONVENTIONAL SUPERCONDUCTOR

The breakthrough experiments that have shaped the understanding of the pairing symmetry focus on the breaking of time reversal symmetry (TRS) in the superconducting state. Specifically, it was found using muon spin resonance experiments and polar Kerr microscopy that internal magnetic fields spontaneously appear below T_c (see Figure 7.1a)[13, 14]. Moreover, using doped samples, with reduced T_c, it was shown that TRS breaking is directly tied to the onset of superconductivity[15]. The breaking of TRS at T_c has an important consequence: the superconducting order parameter is of a two-component nature.[1][16] For the tetragonal lattice of Sr_2RuO_4, i.e., a D_{4h} symmetry point group, this entails either a spin triplet p-wave pairing: $p_x \pm ip_y$ ($S = 1$, $L = 1$), or singlet d-wave pairing: $d_{xz} \pm id_{yz}$ ($S = 0$, $L = 2$).[2] Next, Sr_2RuO_4 was examined by nuclear magnetic resonance (NMR) Knight shift measurements and inelastic neutron scattering experiments, which both measure the spin susceptibility of the electronic system. It was found that spin susceptibility below the critical current is not suppressed, indicating a triplet order parameter (see Figure 7.1b)[17, 18]. Furthermore, using cantilever magnetometry measurements, it was found that mesoscopic rings of Sr_2RuO_4 can host half-quantum vortices under the application of an in-plane magnetic field[19]. This further strengthens the hypothesis of a triplet order parameter, where the Cooper pair spins lie in the ab-plane. Therefore, for a long time, the prime candidate for the pairing symmetry was $p_x \pm ip_y$.

However, some inconsistencies with the chiral p-wave picture remained. First, the upper critical field H_{c2} in the ab-plane is Pauli limited[20]. Pauli limiting behavior results from the balance between superconducting condensation energy (set by the magnitude of the gap) and magnetic polarization energy (set by the spin susceptibility)[21]. If H_{c2} in the ab-plane is Pauli limited, this signifies a suppression of the spin susceptibility below T_c, which is in direct contradiction to the spin susceptibility measurements. Besides, detecting the magnetic fields produced by the proposed edge currents associated with the chiral p-wave pairing using scanning SQUID remained elusive[22].

---

[1] More components are allowed, but less likely as they require more fine-tuning between the components.

[2] These are the lowest orders. In principle, chiral f-wave, chiral h-wave, or even higher orders are allowed, although Occam's razor speaks against them.

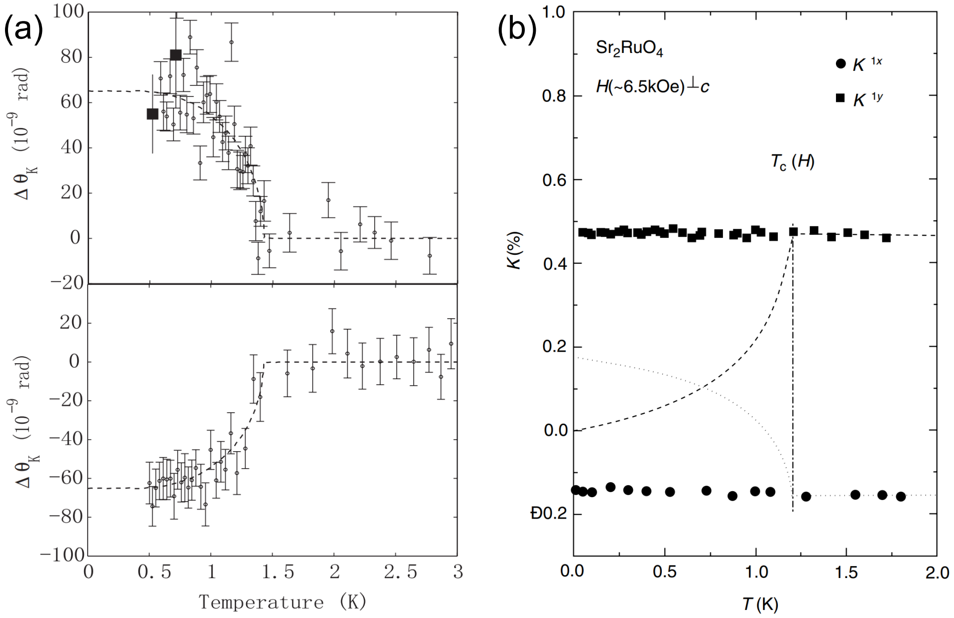

Figure 7.1: Reproduction of two classic results obtained on Sr_2RuO_4. (a) shows a measurement of the magneto-optic Kerr effect, which is the rotation of polarized light reflected on the surface of a Sr_2RuO_4 crystal as a function of temperature. The polarization indicates local magnetism, which only appears below $T_c = 1.5$ K. This result is one of the two main bodies of evidence for a broken TRS superconducting state in Sr_2RuO_4 (the other being muon spin resonance[13]). The sign of the polarization rotation can be controlled by field cooling the sample, as evidenced by the difference between the lower and upper panel, which indicates a chiral pairing. Figure reproduced from ref. [14]. In (b), a measurement of the ^{17}O Knight shift as a function of temperature is shown. This technique measures the spin susceptibility of the electronic system, which was found to be unsuppressed below T_c. Together with work on polarized-neutron scattering[18], this formed strong evidence for a triplet order parameter for over twenty years. Reproduced from ref. [17].

7.2.2. POST-2019 RESULTS: A SHIFT FROM THE p-WAVE PARADIGM

It is not an understatement that our lives changed dramatically at the end of 2019 and the beginning of 2020: the NMR Knight shift experiments on Sr_2RuO_4 were revisited, and it was found that the unsuppressed spin susceptibility was caused by a subtle heating effect of the substrate holder[23, 24]. Likewise, the inelastic neutron scattering measurements were repeated using lower magnetic field pulses and improved statistics, confirming the spin susceptibility suppression below T_c[25]. On the other hand, TRS breaking experiments were also repeated and found still valid. specifically, by applying uniaxial strain to the crystals during muon spin resonance experiments, it was revealed that the critical temperature can be raised even to double its unstrained value, while the temperature at which TRS is broken (T_{TRS}) remained at 1.5 K (see Figure 7.2a)[26]. This was interpreted as a strain-induced increase of T_c of one component of the wave function, whereas the T_c of the second component remained the same at T_{TRS}. Therefore only below T_{TRS} this results in a two-component pairing. Besides, this experiment also shows a clear difference between the intrinsic unstrained supercon-

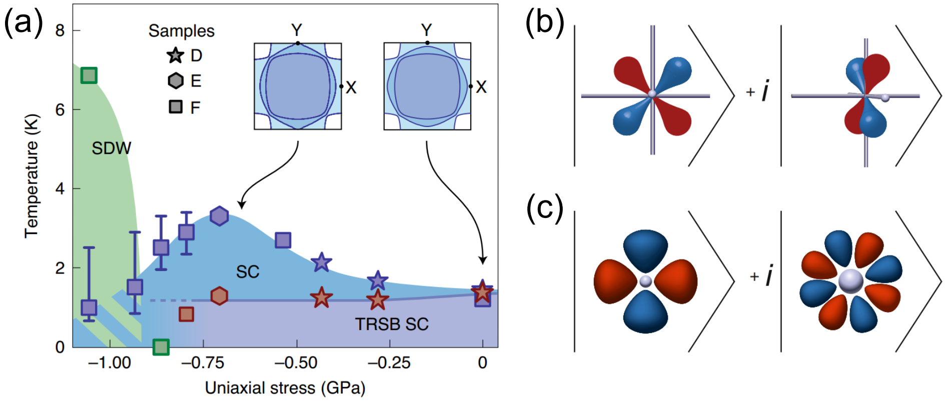

Figure 7.2: (a) phase diagram detailing the time reversal symmetry breaking (TRSB) under the uniaxial stress, as determined by muon spin resonance. Even though the T_c of the superconducting (SC) phase can be more than doubled, T_{TRS} remains 1.5 K. This was interpreted as a rise in critical temperature corresponding to one of the two components of the wave function. At high strain, a spin density wave (SDW) is revealed. The inset shows a schematic of the Fermi surface of Sr_2RuO_4; the origin of the peak in T_c lies in the γ-band passing through a Lifshitz transition near the maximum T_c. Image taken from ref. [26]. (b) and (c) show a schematic representation of the two most likely candidates for the pairing symmetry of Sr_2RuO_4: $d_{xz} \pm i d_{yz}$ and $d_{x^2-y^2} + i g_{xy(x^2-y^2)}$ pairing respectively. The color coding is similar as in Figure 2.2. Images taken from ref. [30].

ducting state and the extrinsic increased-T_c state, coined the ‘3K-phase’. The latter was identified as resulting from strain[27]. In conclusion, this collection of experiments caused a shift away from the p-wave paradigm toward even parity order parameters, with most prominently $d_{xz} \pm i d_{yz}$ pairing, i.e., the chiral d-wave pairing (see schematic in Figure 7.2b).

There is, however, evidence against $d_{xz} \pm i d_{yz}$ pairing, as well. First, from thermal conductivity measurements, it was shown that vertical line nodes exist in the gap structure, which is incompatible with chiral d-wave pairing[28]. Besides, a chiral d-wave state should exhibit a second transition in the heat capacity, tied to T_{TRS}, which can be revealed under uniaxial strain. However, in recent measurements, this second discontinuity was lacking[29].

An alternative route to resolve these issues is by assuming an accidental degeneracy between two single component order parameters. Most notable are the proposals for $s \pm i d_{xy}$ and $d_{x^2-y^2} \pm i g_{xy(x^2-y^2)}$ [31–33]. These, especially the latter, might seem exotic, but they resolve the breaking of TRS with the vertical line node and the missing second discontinuity in the heat capacity. The $s \pm i d_{xy}$ pairing is supported by the strong spin-orbit and Hund’s coupling present in the normal state, resulting in a possibly interorbital triplet pairing that behaves as intraband singlets; therefore, this pairing is coined ‘shadowed triplet’[34, 35]. Furthermore, $d_{x^2-y^2} \pm i g_{xy(x^2-y^2)}$ (see schematic in Figure 7.2c) is compatible with the temperature dependence of the elastic constants in recent ultrasound measurements[36, 37], and the quadratic dependence of $T_{TRS} - T_c$

on uniaxial strain[38], among many other experimental observations[33]. On the other hand, such an accidental degeneracy requires fine-tuning of the material parameters. In other words: in a universe dominated by s-wave and some d-wave superconductors, an accidental degeneracy between d- and g-wave is a *very* major coincidence. More importantly, although uniaxial stress splits T_{TRS} and T_{c}, it was found that hydrostatic pressure induces a downward trend in both, which is highly unlikely for an accidental degeneracy[39]. Finally, neither $d \pm ig$ pairing nor chiral d-wave pairing can account for the observation of half quantum vortices in magnetometry measurements, and the proximity effect in Sr_2RuO_4-SF hybrid structures[3] [19, 41].

Clearly, a plethora of proposed pairing symmetries are found in literature based on seemingly contradicting experimental results. What does that leave us for the *actual* pairing symmetry of Sr_2RuO_4? Maybe the best answer can be found in ref. [39]: "the difficulty in reconciling apparently contradictory experimental results in Sr_2RuO_4 may mean that one or more major, apparently solid results will in time be found to be incorrect, either for a technical reason or in interpretation. Further experiments are therefore necessary." Regardless of the validity of previous experiments, almost all of the work discussed in this section concerns macroscopic crystals. As argued in the introduction, a chiral superconductor can break up into domains, which for Sr_2RuO_4 is supported by numerous studies, for example, by the observation of telegraph noise in Sr_2RuO_4 corner junctions and the sign change in the Kerr signal, during field-cooled experiments[14, 42, 43]. As these are typically micrometer-sized, studying sub-micron devices can lead to experiments on a single domain, or better yet, on a single domain wall separating the two domains. Our first efforts in trapping a single chiral domain wall, published in a previous work, are discussed below.

7.3. TRAPPING A SINGLE SUPERCONDUCTING DOMAIN WALL IN MESOSCOPIC Sr_2RuO_4

In Chapter 6, we described a procedure of fabricating microscopic flakes from a bulk crystal using mechanical exfoliation. Sr_2RuO_4 is well suited to create microstructures using the same method. Therefore, the same procedure is applied for the sample production in this chapter. For a more detailed discussion of the sample production method, see Appendix A of Chapter 6.[4] Specifically, we used this method in a previous work to structure microrings in the exfoliated crystals[6]. Striking about these micro devices, and the ones presented in the rest of this chapter, are their high residual resistivity ratio (RRR) and their bulk T_{c}, indicating that neither the exfoliation method nor the focused ion beam structuring method affects the crystal quality. Besides, since the T_{c} never exceeds 1.5 K, it gives indisputable proof of the absence of the 3K-phase and,

---

[3] Although, within the $d \pm ig$ pairing framework half-quantum vortices can exist, they require a specific varying strain pattern[40].

[4] The crystals were grown using the floating zone method in the group of Y. Maeno[44].

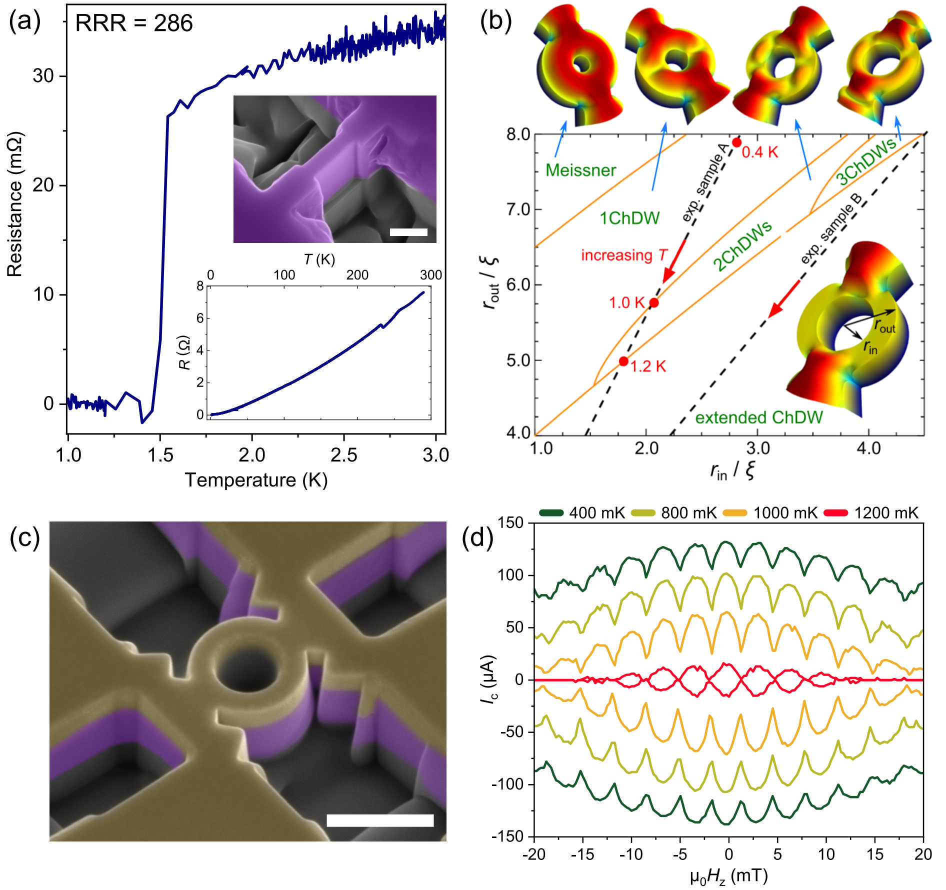

Figure 7.3: (a) Resistance versus temperature of a 200 nm wide constriction in a Sr$_2$RuO$_4$ flake. Despite the mechanical exfoliation and the microstructuring using focused ion beams, the device retained a bulk T_c of 1.5 K and a high residual resistivity ratio. The insets show a false colored scanning electron micrograph of the measured device (the scale bar corresponds to 500 nm) and the same dataset plotted for the full temperature range. (b) shows a phase diagram of chiral domain configurations in a microstructured ring based on time-dependent Ginzburg-Landau simulations of a chiral p-wave order parameter. The outer and inner diameter of the ring, normalized to the coherence length, determine the specific configuration: two chiral domain walls in either arm of the ring are stable over a wide temperature range. In the schematic rings, the color code signifies the Cooper pair density, which illustrates that such domain configuration can act as a SQUID-like system. Figure modified from ref. [6]. Here *exp. sample B* is describing Ring 2, and since sample dimensions of Ring 1 are very similar to those of Ring 2, it can be represented by a very similar line (not plotted here). (c) False colored scanning electron micrograph of Ring 1. The crystal is colored purple, protected by a yellow colored layer of gold. The scale bar corresponds to 1 μm. In (d), the critical current versus perpendicular applied magnetic field ($I_c(B)$) is shown, obtained on Ring 1. Over a large range of temperatures, we observe SQUID-like oscillations, despite the homogeneous crystal.

therefore, any significant strain in these devices[27]. A good example is the resistance versus temperature of the 200 nm wide bar presented in Figure 7.3a. In Appendix A we present an overview of the ring samples used to obtain the data presented in this chapter. Some of the experiments presented in this chapter were carried out at Twente University, Appendix A discusses which ones.

For such clean systems, a uniform superconducting phase is expected. The experimental reality is, therefore, quite surprising: the $I_c(B)$-pattern shows clear oscillations with a period determined by fluxoid quantization corresponding to the area of the ring. Typically this pattern is observed on superconducting quantum interference devices (SQUIDs), which are two Josephson junctions in parallel, creating a doubly connected superconductor in a loop geometry. This means that, once the crystal is cooled below T_c, two Josephson junctions spontaneously appear in each arm of the ring. These oscillations, and therefore the junctions, are present at all temperatures below the transition, even down to 50 mK. A false colored scanning electron micrograph of such ring device is shown in Figure 7.3c[5]; $I_c(B)$ obtained on this sample is shown in Figure 7.3d.

Several trivial mechanisms can produce oscillatory behavior of $I_c(B)$ in clean superconducting systems. The arguments against those are reported in reference [6]; here, we will provide a brief overview. First, if the dimensions of a superconducting device are reduced to below the coherence length ξ, naturally, the order parameter is suppressed, and a constriction (or S−s−S) junction is formed. The feature size (e.g., the width of the arms of the ring) of the samples discussed in this chapter is well above the $\xi_{ab-\mathrm{plane}}$ of Sr_2RuO_4, which equals 66 nm at low temperatures. More importantly, such junctions would exhibit a temperature-dependent current-phase relation that leads to a temperature dependence of the shape of the oscillations, which is not measured in our rings[45]. Furthermore, a constriction junction features a multi-valued current-phase relation, which results in a hysteretic IV-characteristic for $T << T_c$[46]. In our samples, however, the retrapping current equals the critical current for all temperatures. The same argument holds against superconducting persistent currents as the origin of the I_c-pattern: aside from the absence of a temperature-dependent amplitude of the oscillations, also the shape does not match the expected sawtooth-like $I_c(B)$ for persistent currents[47]. In addition, current excited vortices can produce oscillations in I_c, however, only in a temperature range to 5% below T_c, not as low as 50 mK[48]. The device in Figure 7.3c is capped by a layer of gold for protection against FIB-induced damages. However, this layer is shorted by the Sr_2RuO_4 crystal in the superconducting phase and therefore cannot be responsible for I_c oscillations. More importantly, the oscillatory behavior is also present in samples that do not have a metallic but insulating capping layer. Finally, accidental weak links, like inclusions and nano cracks, can be ruled out by the large residual resistivity ratios, absence of 3K-phase, and sharp superconducting transitions, indicating pristine crystals.

Alternatively, these spontaneous weak links can be attributed to the presence of superconducting chiral domain walls pinned in the arms of the ring. In order to strengthen this hypothesis, time-dependent Ginzburg-Landau simulations are presented in ref. [6], assuming a chiral p-wave pairing. These show that mono- and multidomain states

---

[5] This specific device has a layer of gold on top, which was left after a failed lift-off procedure during fabrication of electrical contacts. We made a virtue of necessity by using this gold as a capping layer. Since gold is not superconducting, the charge transport is completely dominated by the Sr_2RuO_4 in the superconducting phase.

are stable in ring structures of these dimensions. Besides, a uniform superconducting state can appear. Tuning the inner and outer radius with respect to the coherence length gives rise to these different states, resulting in a phase diagram, reproduced in Figure 7.3b. Combined with the experimental results, this makes compelling evidence for the presence of chiral domain walls. However, since it is unlikely that the pairing symmetry of Sr_2RuO_4 is chiral p-wave, these results need to be reevaluated in light of the most recent literature. The rest of this chapter will be dedicated to this reevaluation and to more recent experiments on the unusual properties of these domain walls revealed under the application of microwave radiation or in-plane magnetic fields.

7.4. DETECTION OF SHAPIRO STEPS

Although the SQUID oscillations in $I_c(B)$ form strong evidence for domain walls in the arms of the ring, the magnetic fields used in these experiments can alter the domain structure of a chiral superconductor[6]. Obtaining the Shapiro response of the rings can therefore confirm their presence without relying on static magnetic fields. In Figure 7.4a, we show the appearance of Shapiro steps obtained on one of the ring samples, confirming the Josephson coupling. We show their accompanying power dependence in Figure 7.4b. Since Shapiro steps can only originate from the Josephson effect, their detection directly rules out persistent currents or current-excited vortices as the origin of the observed $I_c(B)$ pattern. Note that relatively large microwave powers are needed to produce the results in Figure 7.4. Besides, Shapiro steps are only measured under the application of a few selected frequencies. The latter is presumably tied to the re-

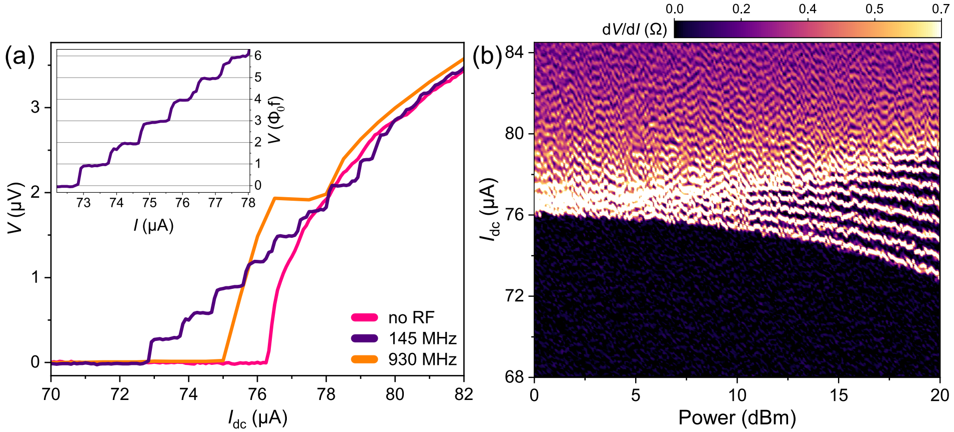

Figure 7.4: Shapiro response obtained on Ring 4. (a) IV-characteristic around I_c for different applied microwave frequencies, obtained at 50 mK and maximum applied power (20 dBm). Clear quantized steps appear near I_c, the height of which linearly scales with the frequency of the applied microwave. The inset shows the data obtained at 145 MHz, rescaled in order to show that the step height matches the expected values for Shapiro steps. In (b), we depict the power dependence of the Shapiro steps obtained at an applied frequency of 145 MHz.

quirement for large microwave powers: for some frequencies, a natural resonance in the cryostat occurs, which results in an amplified local RF field.[6] A possible explanation for the need for high powers is that the bulk superconducting contacts might partially shield the domain walls.

7.5. CONSIDERATIONS ON GEOMETRY

We have investigated the influence of geometry on the domain structure of our devices by obtaining $I_\mathrm{c}(B)$ on both doubly and singly connected samples. First of all, we have produced a sample that is a doubly connected straight bar, with large superconducting reservoirs as contacts. Figure 7.5a shows a false colored scanning electron micrograph of this device; the corresponding $I_\mathrm{c}(B)$ pattern is shown in Figure 7.5b. We find similar SQUID-like oscillations on this sample as on the ring samples. This directly rules out any influence of the contact geometry on the stability of the chiral domain walls. Furthermore, it shows that the chiral domain walls are stable irrespective of the curvature of the arms of the ring. We have also examined singly connected samples of 500 nm wide and multiple micrometer-sized bar devices. These showed neither an oscillatory $I_\mathrm{c}(B)$ nor the appearance of Shapiro steps. Furthermore, the I_c are sharp and well defined, as commonly observed in bulk superconducting samples. Samples that trap a chiral domain wall, on the other hand, exhibit a relatively broad I_c transition. Therefore, we conclude that no junctions are pinned in micrometer-sized bar devices or 500 nm wide constrictions.

In order to isolate and examine only a single junction, we have carried out a second step of FIB processing on the device depicted in Figure 7.3c (Ring 1), during which we cut one of the arms of the ring, changing it into a singly connected sample (see Figure 7.5c). Using the Shapiro response, we verified the Josephson coupling in this singly connected sample and thereby the presence of a chiral domain wall (see Figure 7.6a). We show the corresponding $I_\mathrm{c}(B)$ in Figure 7.5d. We observe a monotonic decay of the critical current for all temperatures, which contradicts the Fraunhofer interference pattern expected for a single junction. However, the period of the oscillations is given by the effective area, which is much smaller than the total area of the ring for a single arm. Naively, we can estimate the effective area by multiplying the width of the arm by the coherence length (typical width of a chiral domain wall). We find the period matching this area to exceed the measured values of the upper critical field of this device. Therefore, it is impossible to acquire more than the middle lobe of the interference pattern.

A closer inspection of the interference pattern is presented in Figure 7.6b. Instead of a Fraunhofer pattern that is cut-off by H_c2, the data is fitted by a Gaussian decay. Such $I_\mathrm{c}(B)$-patterns are generally observed on long diffusive junctions[49–51]. In this

---

[6] This is supported by the fact that different frequencies for different samples give a Shapiro response, although the sample geometry is very similar.

limit, the scatter centers lead to the Andreev bound states tracing many different paths through the junction. By the central limit theorem, the phase difference associated with these trajectories will approach a Gaussian distribution, which manifests itself as a Gaussian interference pattern. Diffusive is, however, not an adjective that is appropriate to describe Sr$_2$RuO$_4$ (N.B., the mean free path in the normal state is larger than the ring diameter). Nevertheless, we conclude from the phase diagram in Figure 7.3b that the domain walls are in the extended regime, implying no direct *line of sight* between the superconducting contacts. This indicates that a similar mechanism based on scattering on the edges of the ring is responsible for the Gaussian interference pattern.

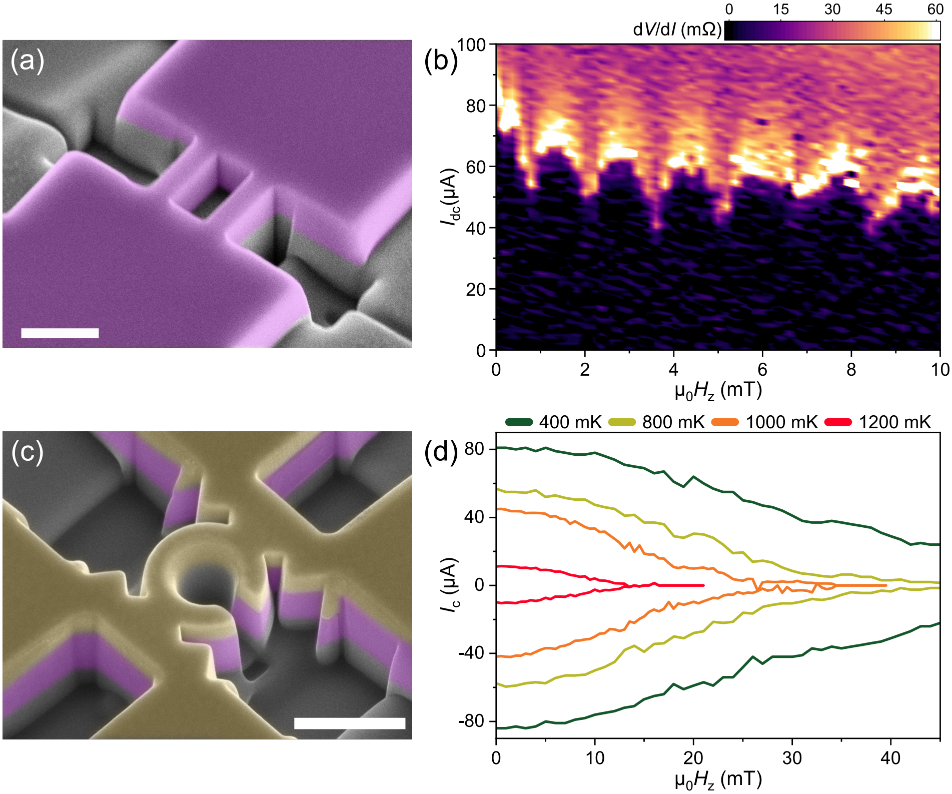

Figure 7.5: (a) a false colored scanning electron micrograph of a doubly connected straight bar sample, called Ring 3. Note that two large superconducting reservoirs form the contacts. Purple indicates the Sr$_2$RuO$_4$ crystal, the SiOx capping layer causes the dark contrast on top of the crystal, and the scale bar corresponds to 1 μm. (b) the $I_c(B)$-pattern, obtained on Ring 3 at 1 K. (c) depicts a false colored scanning electron micrograph of Ring 1 (also shown in Figure 7.3c), where we have cut one arm of the ring, transforming the sample to singly connected. The yellow top layer is the gold protective layer, and purple indicates the Sr$_2$RuO$_4$ crystal. The scale bar corresponds to 1 μm. In (d), we show the $I_c(B)$ patterns obtained on the sample shown in (c) for different temperatures. The critical current decreases monotonically as function of applied field.

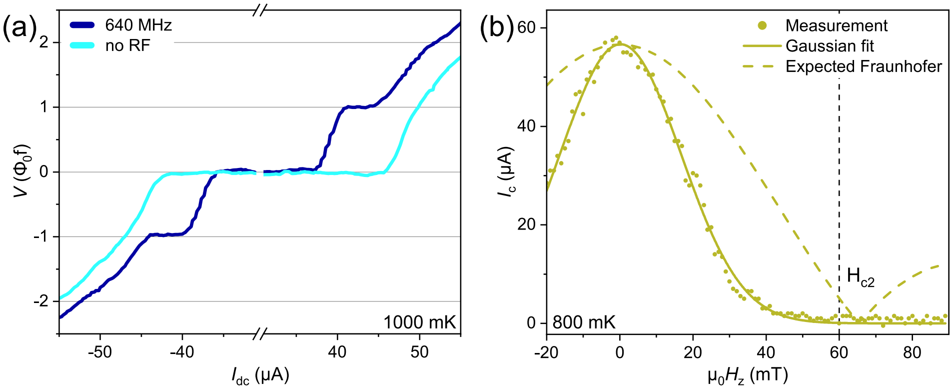

Figure 7.6: (a) Shapiro response of the single arm of Ring 1 (as shown in Figure 7.5c) obtained at 1 K. The voltage is normalized to the expected height of the Shapiro steps at 640 MHz. The Shapiro steps confirm the presence of a chiral domain wall. (b) $I_c(B)$ obtained on Ring 1 at 800 mK. The full circles correspond to the measured data, and the line is a Gaussian fit to the data. The dashed line is the expected Fraunhofer pattern, based on a single Josephson junction with an effective area given by the product of the coherence length and the width of the arm of the ring. The vertical reference line shows the upper critical field defined as $R(H_{c2}) = R_N$. As the chiral domain wall is in the extended regime, the Gaussian $I_c(B)$ can be caused by ballistic scattering processes on the bounds of the arm of the ring.

7.6. $I_c(T)$ OF A CHIRAL DOMAIN WALL JUNCTION

Besides the Shapiro response and the magnetic interference patterns, the temperature dependence of the critical current provides an additional tool to identify the presence of domain walls. In Figure 7.7a, we plot the $I_c R_N$ product of three samples (containing chiral domain walls) with different geometry as a function of normalized temperature. We find that the critical current follows an exponential increase close to T_c, but at lower temperatures, it saturates and plateaus. More importantly, not only the temperature dependence but also the magnitude of $I_c R_N$ is identical for all devices, despite the vastly different sample geometry. Note that we have independently established the presence of domain walls for all the three devices depicted in Figure 7.7a using other techniques (either by the detection of Shapiro steps or the detection of SQUID-like oscillations). From this analysis we conclude that $I_c R_N(T/T_c)$ is universal for chiral domain walls.

In contrast to samples that exhibit the presence of domain walls, devices that lack a chiral domain wall do not show a universal $I_c R_N(T/T_c)$. For example, the two $I_c R_N$-curves shown in Figure 7.7b. Instead of a exponential increase close to T_c, we observe a more bulk-like $(1 - T/T_c)^{1/2}$ dependence.[7] Furthermore, the magnitude of the $I_c R_N$ product is not sample-independent. Typically, the field dependence of the critical current of these samples is a monotonic linear decay, and Shapiro response lacked. In conclusion, the behavior of $I_c R_N(T/T_c)$ allows us to distinguish between samples that effectively pin a chiral domain wall and those that do not.

---

[7] In fact, this same behavior is found in the $I_c R_N(T)$ of the micrometer-sized contacts of samples that exhibit domain walls.

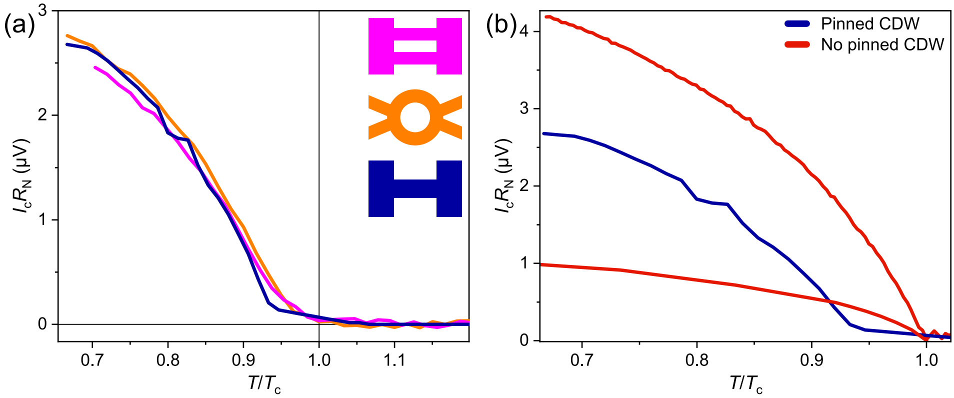

Figure 7.7: $I_cR_N(T/T_c)$ for two classes of samples. (a) samples that do pin chiral domain walls show a universal temperature dependence of I_cR_N, despite there vastly different sample geometry. Here the orange curve corresponds to Ring 2 (T_c = 1.2 K) and the magenta one corresponds to Ring 3 (T_c = 1.28 K). The bar (blue colored curve) has a critical temperature of 1.5 K. Note that not only the temperature dependence, but also the magnitude of I_cR_N is identical between the samples. As a sharp contrast to this behavior, we plot the $I_cR_N(T/T_c)$ of samples that do not exhibit chiral domain walls in (b) with red curves. Here the temperature dependence close to T_c is well captured by the more bulk-like $(1-T/T_c)^{1/2}$ dependence. Furthermore, the magnitude of I_cR_N differs between samples. As reference we plot the curve obtained on the bar sample from (a).

7.7. FIELD-INDUCED BISTABLE DOMAIN CONFIGURATIONS

By applying small in-plane magnetic fields, we found that we can decrease the pinning of the chiral domain walls, which manifests itself as a bistable I_c state controlled by the bias current polarity. This process is shown in Figure 7.8. We find that a high I_c (blue curve) and a low I_c (orange curve) state appears under the application of 20 mT along a line connecting the measurement leads (x-direction). We can switch between these states by applying either a large enough positive or negative current bias, which we denote by I_+ and I_- respectively (indicated by red circles in Figure 7.8). If the sample is in the low I_c configuration, it remains in the low I_c branch until we apply a current larger than I_+. upon passing $I > I_+$, the sample transitions to the high I_c branch, which can be identified by a hysteresis loop on the positive current polarity. The high I_c state is subsequently stable until a negative bias current of $I < I_-$ is applied. Consequently, the sample switches to the low critical current state, resulting in a hysteresis loop on the negative current polarity. Note that both I_c states are exceedingly stable: the hysteresis loops only appear accompanied by switching between the states. Therefore, it is impossible to observe a hysteresis loop multiple times on the same current polarity, making this behavior quite distinct from conventional hysteresis loops in underdamped junctions.

Having made the distinction from conventional hysteresis loops, we recognize that the bistability of I_c results in two hysteresis loops upon cycling the bias current between positive and negative directions (using currents $|I| > \max(I_-, I_+)$). In Figure 7.8, we ob-

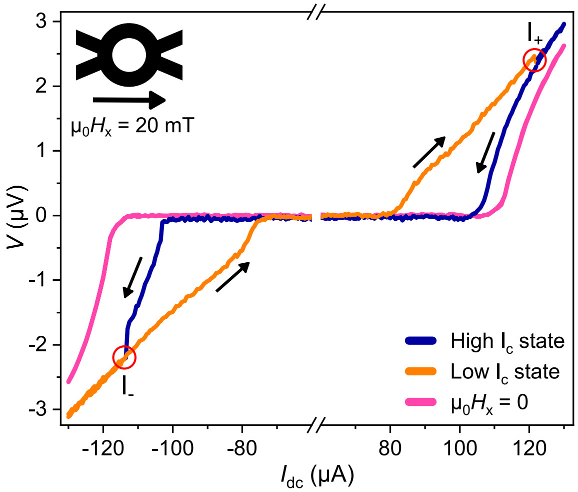

Figure 7.8: IV-characteristics obtained on Ring 2 at 600 mK, under the application of an in-plane field of 20 mT along the x-direction (line connecting the measurement leads attached to the ring). A two-level critical current state is revealed: the blue curve is the high I_c state, and in orange, we plot the low I_c state. As a reference, we show the IV-characteristic for zero field in pink. We can switch between these bistable states by applying high positive or negative bias currents. Specifically, by applying $I > I_+$ (I_+ = 122 μA, for Ring 2), the sample switches to the high I_c state. The reverse is true for a bias current of $I < I_-$ ($I_- = -114$ μA, for Ring 2). Both I_+ and I_- are indicated by red circles. Switching between the I_c states results in a hysteresis loop, the order of which is shown by the black arrows. The switching behavior is characterized by a hysteresis loop of normal order (critical current larger than the retrapping current) on the negative bias polarity and a hysteresis loop of the reversed order on the positive current polarity.

serve a critical current that exceeds the retrapping current when switching from the high I_c state to the low I_c state (on the negative current polarity). However, the reverse is true when switching from the low I_c state to the high I_c state (on the positive current polarity): the retrapping current is higher than the critical current. As this behavior is uncommon, we coin this the anomalous hysteresis polarity. Interestingly, when reversing the field direction, the polarity of the anomalous hysteresis changes sign, as shown in Figure 7.9. In other words, the role of I_+ and I_- in switching between the critical current states interchanges upon reversing the field direction. This is graphically summarized in Figure 7.10.

Before interpreting the bistability I_c property of these samples, first, some general remarks. Although Figures 7.8 and 7.9 are results obtained on ring-shaped devices, we observed this behavior in all samples that pin chiral domain walls, irrespective of curvature or whether they contain singly or doubly connected geometries. Besides, field cooling or applying the field after cooling the sample is cooled below T_c gave identical results. On the other hand, we find that the direction and magnitude of the in-plane magnetic field, required to obtain this behavior, is sample dependent. For example, Ring 1 (Figure 7.3c) showed the bistability of I_c at an in-plane field of 15 mT applied 55 degrees with respect to the x-direction.[8] For a more detailed discussion, the reader is

---

[8] Here the x-direction is defined as *along the ring*; see the inset of Figure 7.8

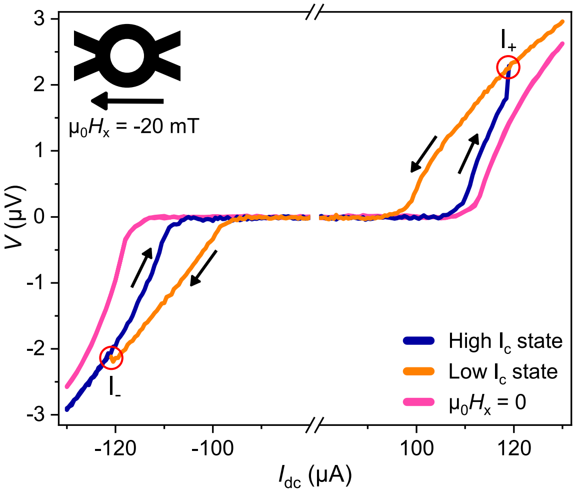

Figure 7.9: Measurements analogous to those presented in Figure 7.8, where the in-plane field direction is reversed. All indicators and symbols are as defined in Figure 7.8 and the data is acquired on Ring 2 at 600 mK. Note that reversing the field direction along the ring, results in an exchange of the role of I_+ and I_- in switching between the critical current states. In other words, the anomalous hysteresis is observed on the negative bias polarity. The values of I_+ and I_- are 119 μA and -121.5 μA respectively.

referred to Appendix B. Note that the magnitude of the field that triggers the bistability is below H_{c1} and can therefore not be caused by in-plane Abrikosov vortices that are mobile in the sample. Finally, this rather unusual switching property cannot be caused by any conventional constriction-type junctions reviewed in section 7.3. Its detection, therefore, reinforces the hypothesis that the spontaneous Josephson coupling in these mesoscopic devices is caused by the presence of superconducting chiral domain walls.

In order to interpret the bistable I_c of our samples, we turn to two key literature results that showed the presence of mobile chiral domain walls. Kidwingira et al. first found evidence of telegraph noise near the critical current of corner junctions on macroscopic crystals of Sr_2RuO_4, which they interpreted as the movement of chiral domain walls[42]. Similarly, Anwar et al. studied Sr_2RuO_4 hybrid junctions between niobium and Sr_2RuO_4 (coupled by a Ru-inclusion to the Sr_2RuO_4 crystal) and found similar hysteresis loops as presented here, along with the aforementioned telegraph noise near I_c (see Figure 7.11a)[43]. Moreover, Anwar et al. found that the application of small fields in the ab-plane increases the telegraph noise near I_c, which indicates that the domain walls become less strongly pinned due to the in-plane fields (see Figure 7.11b). Most likely, the two-level I_c property shares its origins with the telegraph noise observed on macroscopic samples. Both Kidwingira et al. and Anwar et al. discuss macroscopic devices that do not pin domain walls due to the sample size. However, here we study confined structures exhibiting stronger pinning, and therefore the domain configuration is more stable. However, the application of in-plane fields decreases the domain wall pinning, which consequently leads to the appearance of a bistable domain configura-

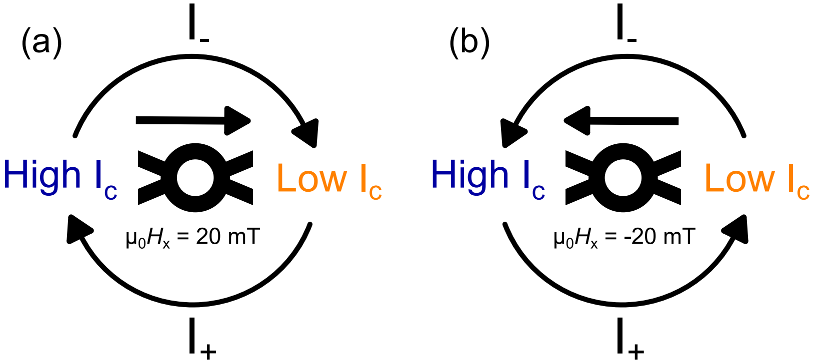

Figure 7.10: Schematic of the interplay between field direction, I_+ and I_- in determining the low or high I_c state in ring structures of Sr_2RuO_4 as revealed under the application of in-plane fields. (a) and (b) correspond to the results presented in Figure 7.8 and 7.9 respectively. The color coding of the high and low critical current states corresponds to the curve color in the IV-characteristics of Figure 7.8 and 7.9. As evidenced by the difference between (a) and (b), reversing the field direction, interchanges the role of I_+ and I_- in changing between the two different I_x states.

tion. In turn, a different domain configuration can lead to a different I_c; the application of an in-plane magnetic field can lead to a bistable I_c in our mesoscopic devices[52]. Not only fields can move the domain walls: as evidenced by the telegraph noise near I_c the bias current also couples to the domain configuration. This explains the influence of I_+ and I_- in switching between the two I_c states. Moreover, if both an electrical current and an in-plane magnetic field can exert a torque on the domain wall, it explains why reversing the field direction interchanges how I_+ and I_- determine the low or high I_c state.

There are, however, also some open questions that remain. First and foremost, how the domain structure is influenced under in-plane fields is not known. More specifically, what is not known is the direction of the lattice vectors with respect to the applied magnetic field, and therefore the possible importance of field-to-lattice alignment. In Appendix C we present, as an outlook, an experiment that determines the a- and b-axis in a mesoscopic device in situ. Secondly, the results presented here raise the question of how a charge current couples to the chiral domain walls and why chiral domain walls can become unpinned by the application of in-plane fields. Thirdly, it must be noted that magnetic fields of the same magnitude were used in the magnetometry experiments that revealed the presence of half-quantum vortices in mesoscopic rings of Sr_2RuO_4[19]. This calls for a reexamination of these results and a possible reinterpretation based on chiral domain walls present in these rings.

Finally, these domain wall junctions can function as superconducting memory elements. Analogous to the devices presented in Chapter 5, we can specify a read-out current between the critical current of the low I_c branch and I_+. This leads to a finite voltage in the low I_c state, whereas a zero voltage in the high I_c state. It is advantageous that the bias current polarity controls the writing procedure of such memory instead of applying a magnetic field. On the other hand, the memory of our rings is limited by the need for finite static magnetic fields and sub-1.5K temperatures. Besides, chiral domain walls can never form non-volatile memories, as they are tied to the superconducting phase.

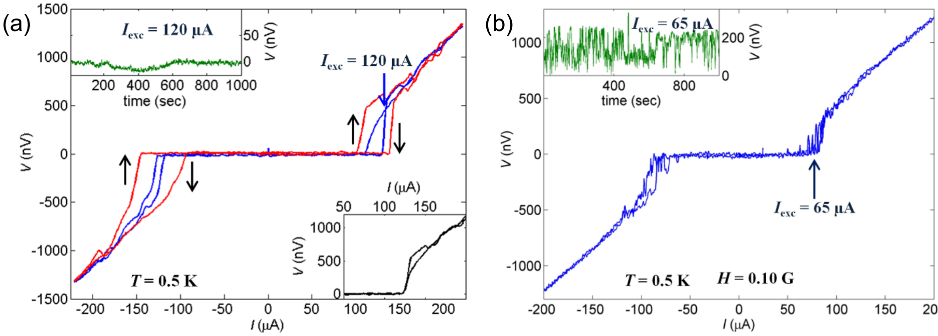

Figure 7.11: Two examples of multistable I_c states, taken from Anwar et al[43]. In (a), there is a clear bistable behavior, with an anomalous hysteresis on the positive current bias and a regular hysteresis loop on the negative bias, comparable to the data in Figure 7.8. As this concerns a macroscopic crystal, the chiral domain walls are pinned less. Therefore, switching between chiral domain configurations does not require the application of in-plane fields. Moreover, the IV-characteristic can be altered between different cooling cycles, indicating a non-deterministic domain configuration when entering the superconducting state. When small magnetic fields are applied in the ab-plane (0.01 mT), the pinning of chiral domain walls decreases, and the domains reconfigure without applying currents larger than I_+ or I_-, resulting in large amounts of telegraph noise near I_c.

7.8. ALTERING THE PERIODICITY OF CURRENT-PHASE RELATION WITH IN-PLANE MAGNETIC FIELDS

Besides a current switchable bistable I_c state, in-plane fields can alter the periodicity of the current-phase relation associated with the domain wall junctions. We found that some combinations of field magnitude and alignment can give rise to clear half-integer Shapiro steps, which indicates a current-phase relation that is π-periodic instead of 2π-periodic. For example, in Figure 7.12a, we plot both I_c states of Ring 4, corresponding to the application of a 10 mT field along the x-direction. We find the bistable I_c states where the high I_c branch shows only an integer Shapiro response, whereas the low I_c branch shows both integer and half-integer steps. This suggests that the two I_c states have different current-phase relations. Upon resetting the field (i.e., diminishing the field to zero and subsequently reapplying the original field), we find that the domain composition is reconfigured (see Figure 7.12). This results in a missing first Shapiro step on the positive current polarity, and on the reverse sweep, after switching to the low I_c state, the appearance of half-integer steps, where the first half step is missing. Furthermore, the half-integer Shapiro response seems limited to one current polarity. Although we did not find a direct correlation between the occurrence of the anomalous hysteresis loop and the non-integer steps, reversing the field direction changes the po-

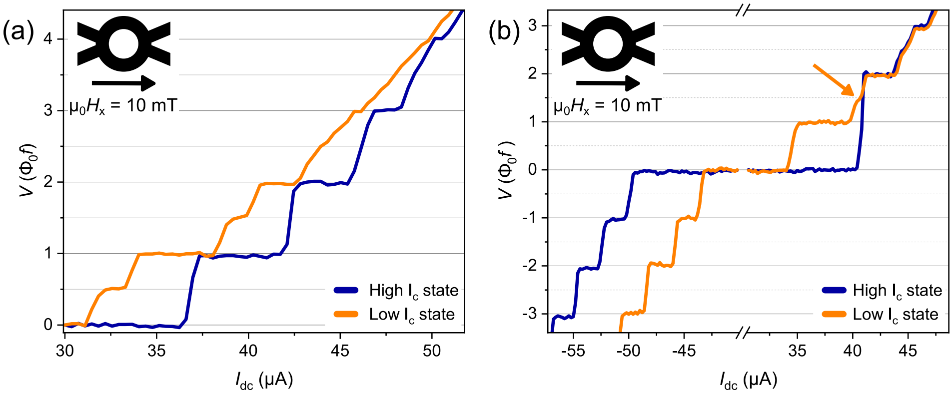

Figure 7.12: IV-characteristics acquired under simultaneous radiation of microwaves (145 MHz) and the application of an in-plane field of 10 mT along the x-direction on Ring 4 at 50 mK. In (a), we observe the unmistakable appearance of half-integer Shapiro steps in the low I_c state. However, the high I_c state only shows an integer Shapiro response, indicating an altered current-phase relation between the I_c states. After resetting the field (i.e., setting the field to zero and subsequently reapplying the same field), we only find integer Shapiro steps on the negative current polarity. The first step is lacking on the positive bias polarity; only in the low I_c state do we observe a half-integer Shapiro step, indicated by the yellow arrow..

larity at which we observe the fractional steps. Therefore, most likely, there is a relation between the multistable I_c states and the appearance of the fractional Shapiro steps: both properties require similar in-plane fields, and the exact magnitude or orientation seems to vary between samples. Moreover, there seems to be no correspondence between the geometry of the sample and the field direction required to trigger either the two-level I_c property or the non-integer Shapiro steps.

To examine the origin of the fractional Shapiro steps, we perform a magnetic field sweep under microwave radiation (see Figure 7.13). Before this experiment, we verified a reproducible half-integer Shapiro response at finite in-plane fields. We observe a Fraunhofer-like interference pattern with Shapiro steps close to I_c. In Figure 7.13b,c we plot IV-characteristics at specific fields, extracted from Figure 7.13a. Interestingly, $\frac{1}{3}$-fractional Shapiro steps appear near the minima of the interference pattern (i.e., 4.5 mT and 9.9 mT). Naturally, at these minima, the first harmonic of the current-phase relation is suppressed, and therefore it can be dominated by the higher harmonics. This effect is commonly observed in, for example, $0-\pi$ transitions in SF-hybrid junctions[53, 54]. Beyond 15 mT, however, there seem to be no oscillations in the $I_c(B)$-pattern. In this regime, we see the appearance of the half-integer steps, which might be distinguished from the trivial fractional steps observed in the minima of $I_c(B)$. At even higher magnetic fields, the half-integer steps disappear, and only integer steps are observed. Besides, integer steps are observed between the minima in the oscillatory part of the $I_c(B)$-pattern.

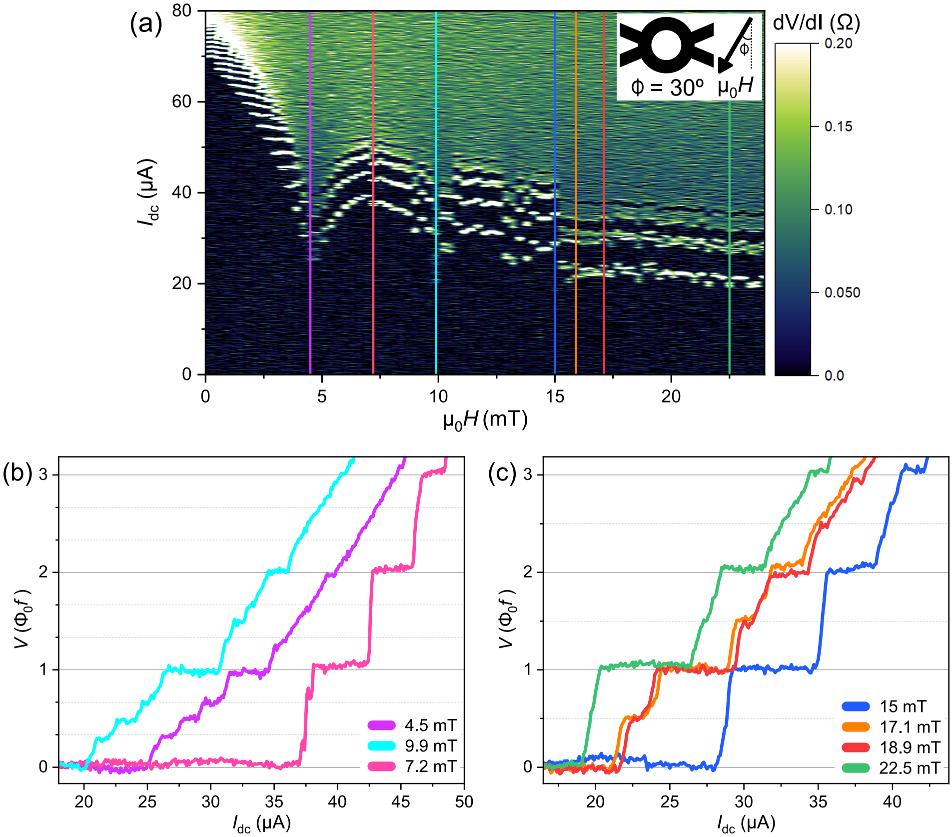

Figure 7.13: (a) In-plane magnetic field sweep obtained on Ring 4, under the application of microwaves (145 MHz) at 50 mK. There is a 30 degree angle between the y-axis and the magnetic field direction (see inset). To erase any field history, we reduce the field to zero between each field step and we cycle both current polarities twice at each field. In (a) we plot the up-sweep of the second cycle (i.e., increasing current direction). (b) and (c) show IV-characteristics extracted from (a). The color coding of the vertical reference lines corresponds to the color of the curves in (b) and (c).

The period of the oscillations in $I_c(B)$, combined with the thickness of the crystal, implies a junction length of 1.5 µm, which exceeds the outer diameter of the ring of 1 µm. This is not expected since the interference pattern is obtained at 50 mK. No extended domain wall regime is expected at these temperatures and sample dimensions, according to the time-dependent Ginzburg-Landau simulations. Furthermore, in-plane magnetic field sweeps obtained on other ring samples never exhibited a Fraunhofer-like pattern but rather a monotonic decay. The interference pattern presented in Figure 7.13a, therefore, raises the question of what the junction geometry is and how it is related to the domain wall structure. The interference pattern also seems to suggest that the $\frac{1}{3}$-fractional Shapiro steps result from a trivial process. On the other hand, since they are stable over a larger field range, the half-integer Shapiro response might be the consequence of a more profound effect of the presence of in-plane fields.

7.9. IMPLICATIONS FOR THE PAIRING SYMMETRY

As mentioned in the introduction, the chiral p-wave pairing paradigm became problematic in recent years due to multiple revisited experiments, and today the proposals range far and wide. This section will try to reconcile our experiments with one of those proposals.

Since the discovery of SQUID-like oscillations in homogeneous rings of Sr_2RuO_4 reported in [6], and their attribution to chiral domain walls, we have studied numerous properties of these remarkable junctions. To explicitly name them: the temperature dependence associated with the trapping of a domain wall, which is sample independent; the influence of geometry on the domain structure; the bistability of chiral domain walls by the application of in-plane magnetic fields, and the alteration of the periodicity of the current-phase relation due to said in-plane fields. Before continuing the discussion of the consequences of these observations, we conclude that these unusual properties can never occur in regular constriction type junctions nor as a result of persistent currents. Therefore, the experiments presented in this chapter form a compelling collection of evidence for the existence of superconducting domains in Sr_2RuO_4.

Chiral p-wave superconductivity is one of the least complex symmetries featuring the spontaneous appearance of superconducting domains. However, since chiral p-wave pairing has become an unlikely candidate for describing the pairing in Sr_2RuO_4, we require an alternative featuring such domains. Naturally, any chiral order parameter satisfies this need. Alternatively, as mentioned in section 7.2.2, there is a proposed class of superconducting pairings composed of two single-component order parameters. Although these order parameters can also break up into superconducting domains, this does not happen spontaneously. Instead, a varying strain texture caused by dislocations and impurities is required for the stabilization of the domain walls[40, 55]. Not only is this scenario opposed by our evidence of clean and strain-free crystals, it also suggests that the domains are set by the lattice and therefore are not mobile, which is directly contradicted by our in-plane field experiments. On the other hand, a symmetry-protected chiral pairing allows for mobile domains. Therefore, chiral d-wave is a more likely candidate based on our experiments.

In section 7.2.2 we noted two arguments countering the chiral d-wave picture. First is the observation of vertical line nodes, which seems to conflict with chiral d-wave pairing, for which horizontal line nodes are expected[28]. However, taking into account spin-orbit coupling and inter-layer interactions (as opposed to a more simple two-dimensional model), it was shown that a chiral d-wave superconductor can exhibit quasi-particle Fermi surfaces, which can appear as vertical line-nodes in experiments[56, 57]. The missing second transition in heat capacity measurements poses a bigger problem, which, up to now, remains unresolved[29].

7.10. CONCLUSION AND OUTLOOK

We have studied the properties of mesoscopic structures of $\mathrm{Sr_2RuO_4}$ in various singly and doubly connected microstructures and found the spontaneous emergence of Josephson junctions, independent of the sample geometry in the superconducting phase. This is supported by the measurement of the $I_\mathrm{c}(B)$-pattern, as well as a clear Shapiro response. Furthermore, we find that the $I_\mathrm{c}R_\mathrm{N}$ product displays a universal temperature dependence, regardless of device geometry. Under the application of in-plane fields, a bistable critical current emerges, characterized by a low I_c and a high I_c state that can be switched by the application of electrical current. Besides, in-plane fields alter the periodicity of the current-phase relation of the spontaneous junctions, which is reflected by the appearance of half-integer steps in the Shapiro response. Combining these unusual observations provides compelling evidence for the presence of superconducting domains in $\mathrm{Sr_2RuO_4}$. Naturally, a chiral order parameter can feature such domains, and in light of the recent experimental work detailing the pairing symmetry of $\mathrm{Sr_2RuO_4}$, a chiral d-wave order parameter of the form $d_{xz} \pm i d_{yz}$, is, therefore, the most promising candidate.

The experiments presented in this chapter raise plenty of questions as well. For example, why are the domain walls more mobile under the application of in-plane fields, and what determines their interaction with charge current? Besides, what determines the direction and magnitude of the in-plane magnetic fields required to produce the bistable I_c and likewise the half-integer Shapiro response? Finally, how are these effects related to the alignment of the crystalline axes? These questions remain unanswered. Besides, there remain multiple apparent contradictory results in literature. Therefore, further experiments are necessary.

APPENDICES

A. SAMPLE DIMENSIONS OF RING SAMPLES

In this Appendix, we provide an overview of the length parameters of the different samples used to obtain the data in this chapter. They are summarized in Table 7.1. Note that the behavior reported on each sample is not exclusive to that specific device. Besides, some of the data is not acquired in the Vectormagnet (see Appendix A of Chapter 2) but at Twente university in a dilution refrigerator capable of reaching 10 mK base temperatures. The data shown in Figures 7.4, 7.12, 7.13, B.1, and B.2 are obtained using a Stanford Research Instruments SR830 lock-in in Twente using a similar method as described in Appendix A of Chapter 2.

B. STABILITY OF CHIRAL DOMAIN WALLS UNDER IN-PLANE FIELDS

Although the mobile domain walls and their associated bistability of the critical current are observed universally in all samples, the direction and magnitude of the in-plane field required to trigger this behavior vary between samples. This Appendix presents an extensive search for the I_c bistability in the in-plane field parameter space obtained on two different ring samples.

In order to quantify the amount of hysteresis in an IV-characteristic, which accompanies switching between different I_c states, we define a parameter that measures the absolute voltage difference between the low I_c state and the high I_c state. We calculate this parameter by summing the absolute voltage difference between the two states at each current:

Sample name	D_{in}	D_{out}	t	Comments
Ring 1	0.608 µm	1.20 µm	0.450 µm	This sample is shown in the false colored scanning electron micrographs of Figure 7.3c and Figure 7.5c. It has a thick conducting gold capping layer. It is used to obtain the interference patterns depicted in Figure 7.3d, Figure 7.5d and 7.6.
Ring 2	0.531 µm	1.26 µm	0.7 µm	Sample presented in reference [6] as 'Exp. sample B' (see Figure 1d in ref. [6] for an scanning electron micrograph). The geometry of this sample is very close to Ring 1. We obtained the data presented in section 7.7 on this sample as well as $I_c(T)$ data.
Ring 3	0.475 µm	1.38 µm	0.589 µm	This is the doubly connected bar sample shown in the false colored scanning electron micrograph of Figure 7.5a. The sample is composed of two 1 µm long bars; here, the inner diameter references the distance between the bars, and the outer diameter is the total width of the sample (i.e., the inner diameter plus the width of both bars). This sample provided the data for the $I_c(T)$ and the interference pattern in Figure 7.5b.
Ring 4	0.486 µm	1.01 µm	0.253 µm	This sample is shown in the false colored scanning electron micrograph of Figure C.1b. The ring part of the sample is used to obtain the Shapiro step results presented in Figure 7.4, 7.12 and 7.13. Besides, we studied the stability of the critical current state switching on this sample (i.e., Figure B.2).

Table 7.1: Table containing the dimensions (inner diameter D_{in}, outer diameter D_{out} and the thickness t) and other details of the ring samples used acquire the data presented in this chapter.

$$\text{Hyst.} = \sum_{I_i} |V(I_i \rightarrow) - V(I_i \leftarrow)| \tag{7.1}$$

Here we sum over each current probed in the IV-characteristic, $V(I_i \rightarrow)$ is the voltage measured during the forward sweep, and $V(I_i \leftarrow)$ the voltage measured on the reverse sweep. Naturally, this parameter gives a measure for the surface enclosed by the hysteresis loops: it is zero if there is no hysteresis and finite if any hysteresis exists between the current and retrapping current. In Figure B.1 we plot the hysteresis parameter for a large combination of field magnitudes and directions. Here ϕ is the polar angle in the xy-plane, and $\phi = 0$ corresponds to the direction along the ring, as defined in the inset of Figure 7.8. We find $\phi = 20$ degrees the optimal angle to produce the switching behavior reported in section 7.7.

In Figure B.2a, we present a measurement of the same hysteresis parameter for Ring 4, which does not have any preferential angle along which it produces the bistable I_c states. Moreover, we have obtained the IV-characteristic at each field twice, which allows us to examine the reproducibility of the hysteresis parameter at a constant magnetic field (see Figure B.2b). From the difference between Figure B.2a and B.2b, we can conclude that this sample pins chiral domain walls less effectively than other samples. Note that this does not mean the sample can be regarded as irregular, as it showed a

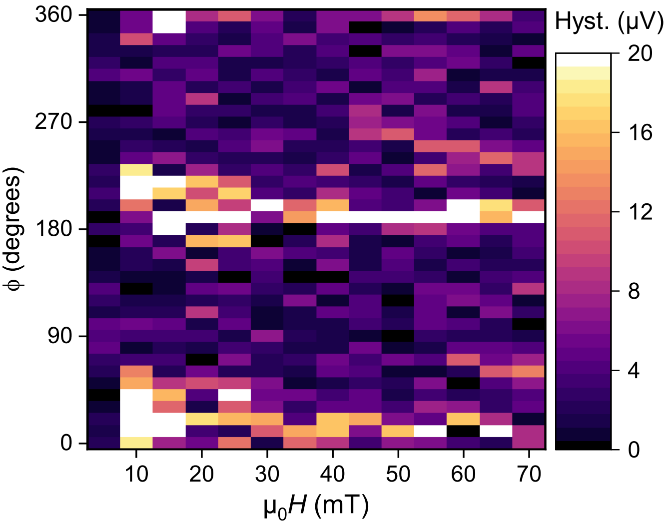

Figure B.1: Hysteresis parameter (summed difference between the high I_c state and the low I_c state) extracted for different combinations of field magnitude and direction. Note that each pixel represents a single IV-characteristic. Here ϕ is the polar angle in the xy-plane (with the x direction along the ring, as defined in Figure 7.8). At $\phi = 20$ degrees we find clear hysteresis behavior, indicating switching between different I_c states (i.e., mobile domain walls). Before setting each field and starting the IV-measurement, the field was reduced to zero.

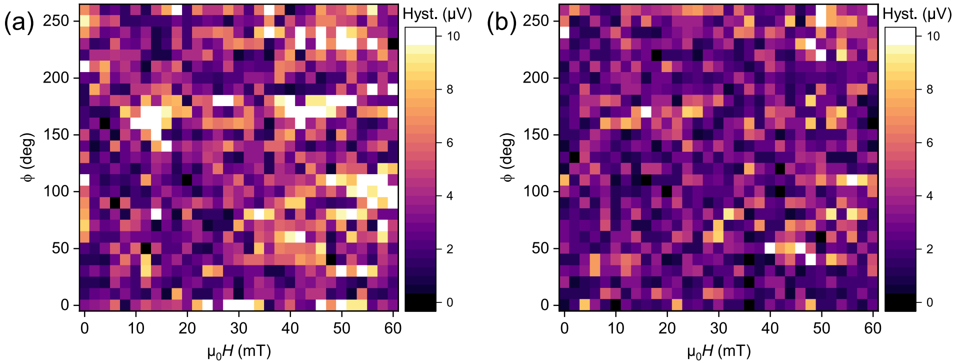

Figure B.2: (a) The same quantity measured as presented in Figure B.1 for Ring 4. The same measurement protocol was used to acquire the data. However, the IV-characteristic was measured twice at each field. In (b), we plot the hysteresis parameter obtained from the second IV-characteristic. This sample does not have a preferred field direction that triggers the mobile domain regime. Besides, this sample pins the chiral domain walls less effectively, which can be seen from the difference between (a) and (b): the hysteresis loops are less reproducible.

clear SQUID-like interference pattern and Shapiro response.

C. PROPOSED EXPERIMENT TO ESTABLISH A- AND B-AXIS IN SITU

Since we found no correlation between the geometry of the samples and the field alignments that trigger the critical current bistability, comparing the relative field directions to the orientation of the atomic lattice would provide valuable insight into the underlying mechanism. There might be a relation to the nematicity of the electronic system found in the normal state of Sr_2RuO_4 [58], if there is no correlation with the atomic lattice. As an outlook, we provide an experiment, that can establish the direction of the a- and b-axis of the crystal flake in situ.

Crucial to this proposal is the observation of an anisotropy in the upper critical field in the ab-plane of Sr_2RuO_4 (see Figure C.1a) [59]. During this experiment, the orientation of the lattice was established first, and the anisotropy was measured. We propose to utilize the reverse: measure the anisotropy in H_{c2} and infer the direction of the principle axes from this measurement using the results presented in reference [59]. Figure C.1b depicts a sample shaped into a multiple micrometer-sized bar attached to a ring with a diameter of 1 μm. Using contacts V_1 and V_2, we can measure the voltage over the bar, which does not pin chiral domain walls due to its relatively large size. Therefore we can assess the anisotropy in H_{c2} and establish the crystalline axes of the flake. Since there is a fixed orientation between the bar and the ring, this information transfers to the ring. Next, we can switch our voltage measurement to contacts V_2 and V_3, which measure the voltage over the ring, allowing us to repeat the experiments using in-plane fields and relate them to the crystalline lattice.

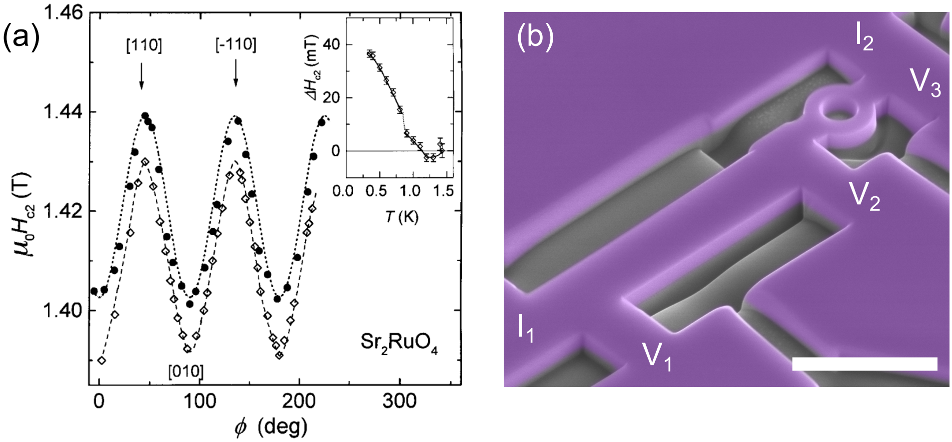

Figure C.1: (a) the upper critical field of Sr_2RuO_4 in the ab-plane as a function of the polar angle between the field direction and the a-axis, taken from reference [59]. Using this result, we can infer the crystalline axes by measuring the anisotropy in H_{c2}. (b) false colored scanning electron micrograph of a sample that can be employed to carry out the proposed experiment. Current is applied between the contacts labeled with I_1 and I_2. The bar part of this sample (between voltage contacts V_1 and V_2) is relatively large and therefore does not pin chiral domain walls. We can use the bar to measure the anisotropy in H_{c2}, which then provides information about the crystalline axes of both the bar and the ring (experimentally accessible using contacts V_2 and V_3). The scale bar corresponds to 2 μm; this sample was used to obtain the Shapiro data presented in the main text.

REFERENCES

[1] Hardy, W. N., Bonn, D. A., Morgan, D. C., Liang, R. & Zhang, K. Precision measurements of the temperature dependence of λ in $YBa_2Cu_3O_{6.95}$: Strong evidence for nodes in the gap function. *Phys. Rev. Lett.* **70**, 3999–4002 (1993).

[2] Wollman, D. A., Van Harlingen, D. J., Lee, W. C., Ginsberg, D. M. & Leggett, A. J. Experimental determination of the superconducting pairing state in YBCO from the phase coherence of YBCO-Pb dc SQUIDs. *Phys. Rev. Lett.* **71**, 2134–2137 (1993).

[3] Tsuei, C. C. *et al.* Pairing symmetry and flux quantization in a tricrystal superconducting ring of $YBa_2Cu_3O_{7-\delta}$. *Phys. Rev. Lett.* **73**, 593–596 (1994).

[4] Bednorz, J. G. & Müller, K. A. Possible high T_c superconductivity in the Ba−La−Cu−O system. *Z. Phys. B Con. Mat.* **64**, 189–193 (1986).

[5] Sigrist, M. & Agterberg, D. F. The role of domain walls on the vortex creep dynamics in unconventional superconductors. *Progr. Theor. Phys.* **102**, 965–981 (1999).

[6] Yasui, Y. *et al.* Spontaneous emergence of Josephson junctions in homogeneous rings of single-crystal Sr_2RuO_4. *npj Quantum Mater.* **5**, 21 (2020).

[7] Maeno, Y. *et al.* Superconductivity in a layered perovskite without copper. *Nature* **372**, 532–534 (1994).

[8] Mackenzie, A. P. *et al.* Extremely Strong Dependence of Superconductivity on Disorder in Sr_2RuO_4. *Phys. Rev. Lett.* **80**, 161–164 (1998).

[9] Rice, T. M. & Sigrist, M. Sr_2RuO_4: an electronic analogue of ^{3}He? *J. Phys.: Condens. Matter* **7**, L648 (1995).

[10] Rice, M. An analogue of superfluid ^{3}He. *Nature* **396**, 627–628 (1998).

[11] Maeno, Y., Kittaka, S., Nomura, T., Yonezawa, S. & Ishida, K. Evaluation of spin-triplet superconductivity in Sr_2RuO_4. *J. Phys. Soc. Japan* **81**, 1–29 (2012).

[12] Mackenzie, A. P., Scaffidi, T., Hicks, C. W. & Maeno, Y. Even odder after twenty-three years: The superconducting order parameter puzzle of Sr_2RuO_4. *npj Quantum Mater.* **2**, 40 (2017).

[13] Time-reversal symmetry-breaking superconductivity in Sr_2RuO_4. *Nature* **394**, 558–561 (1998).

[14] Xia, J., Maeno, Y., Beyersdorf, P. T., Fejer, M. M. & Kapitulnik, A. High resolution polar kerr effect measurements of Sr_2RuO_4: evidence for broken time-reversal symmetry in the superconducting state. *Phys. Rev. Lett.* **97**, 167002 (2006).

[15] Luke, G. *et al.* Unconventional superconductivity in Sr_2RuO_4. *Phys. B: Condens. Matter* **289-290**, 373–376 (2000).

[16] Sigrist, M. & Ueda, K. Phenomenological theory of unconventional superconductivity. *Rev. Mod. Phys.* **63**, 239–311 (1991).

[17] Ishida, K. *et al.* Spin-triplet superconductivity in Sr_2RuO_4 identified by ^{17}O Knight shift. *Nature* **396**, 658–660 (1998).

[18] Duffy, J. A. *et al.* Polarized-Neutron Scattering Study of the Cooper-Pair Moment in Sr_2RuO_4. *Phys. Rev. Lett.* **85**, 5412–5415 (2000).

[19] Jang, J. *et al.* Observation of half-height magnetization steps in Sr_2RuO_4. *Science* **331**, 186–188 (2011).

[20] Deguchi, K., A. Tanatar, M., Mao, Z., Ishiguro, T. & Maeno, Y. Superconducting double transition and the upper critical field limit of Sr_2RuO_4 in parallel magnetic fields. *J. Phys. Soc. Japan* **71**, 2839–2842 (2002).

[21] Clogston, A. M. Upper limit for the critical field in hard superconductors. *Phys. Rev. Lett.* **9**, 266–267 (1962).

[22] Hicks, C. W. *et al.* Limits on superconductivity-related magnetization in Sr_2RuO_4 and $PrOs_4Sb_{12}$ from scanning SQUID microscopy. *Phys. Rev. B* **81**, 214501 (2010).

[23] Pustogow, A. *et al.* Constraints on the superconducting order parameter in Sr_2RuO_4 from oxygen-17 nuclear magnetic resonance. *Nature* **574**, 72–75 (2019).

[24] Ishida, K., Manago, M., Kinjo, K. & Maeno, Y. Reduction of the ^{17}O Knight shift in the superconducting state and the heat-up effect by NMR pulses on Sr_2RuO_4. *J. Phys. Soc. Japan* **89**, 034712 (2020).

[25] Petsch, A. N. *et al.* Reduction of the spin susceptibility in the superconducting state of Sr_2RuO_4 observed by polarized neutron scattering. *Phys. Rev. Lett.* **125**, 217004 (2020).

[26] Grinenko, V. *et al.* Split superconducting and time-reversal symmetry-breaking transitions in Sr_2RuO_4 under stress. *Nat. Phys.* **17**, 748–754 (2021).

[27] Steppke, A. *et al.* Strong peak in Tc of Sr_2RuO_4 under uniaxial pressure. *Science* **355** (2017).

[28] Hassinger, E. *et al.* Vertical line nodes in the superconducting gap structure of Sr_2RuO_4. *Phys. Rev. X* **7**, 011032 (2017).

[29] Li, Y.-S. *et al.* High-sensitivity heat-capacity measurements on Sr_2RuO_4 under uniaxial pressure. *Proc. Natl. Acad. Sci. U.S.A.* **118**, e2020492118 (2021).

[30] Agterberg, D. F. The symmetry of superconducting Sr_2RuO_4. *Nat. Phys.* **17**, 169–170 (2020).

[31] Rømer, A. T., Hirschfeld, P. J. & Andersen, B. M. Superconducting state of Sr_2RuO_4 in the presence of longer-range Coulomb interactions. *Phys. Rev. B* **104**, 064507 (2021).

[32] Scaffidi, T. Degeneracy between even- and odd-parity superconductivity in the quasi-1D Hubbard model and implications for Sr_2RuO_4 (2020). Preprint at https://arxiv.org/abs/2007.13769.

[33] Kivelson, S. A., Yuan, A. C., Ramshaw, B. J. & Thomale, R. A proposal for reconciling diverse experiments on the superconducting state in Sr_2RuO_4. *npj Quantum Mater.* **5**, 43 (2020).

[34] Clepkens, J., Lindquist, A. W. & Kee, H.-Y. Shadowed triplet pairings in hund's metals with spin-orbit coupling. *Phys. Rev. Research* **3**, 013001 (2021).

[35] Clepkens, J., Lindquist, A. W., Liu, X. & Kee, H.-Y. Higher angular momentum pairings in interorbital shadowed-triplet superconductors: Application to Sr_2RuO_4. *Phys. Rev. B* **104**, 104512 (2021).

[36] Ghosh, S. *et al.* Thermodynamic evidence for a two-component superconducting order parameter in Sr_2RuO_4. *Nat. Phys.* **17**, 199–204 (2021).

[37] Benhabib, S. *et al.* Ultrasound evidence for a two-component superconducting order parameter in Sr_2RuO_4. *Nat. Phys.* **17**, 194–198 (2021).

[38] Watson, C. A., Gibbs, A. S., Mackenzie, A. P., Hicks, C. W. & Moler, K. A. Micron-scale measurements of low anisotropic strain response of local T_c in Sr_2RuO_4. *Phys. Rev. B* **98**, 094521 (2018).

[39] Grinenko, V. *et al.* Unsplit superconducting and time reversal symmetry breaking transitions in Sr_2RuO_4 under hydrostatic pressure and disorder. *Nat. Commun.* **12** (2021).

[40] Yuan, A. C., Berg, E. & Kivelson, S. A. Strain-induced time reversal breaking and half quantum vortices near a putative superconducting tetracritical point in Sr_2RuO_4. *Phys. Rev. B* **104**, 054518 (2021).

[41] Anwar, M. S. *et al.* Observation of superconducting gap spectra of long-range proximity effect in $Au/SrTiO_3/Sr_1RuO_3/Sr_2RuO_4$ tunnel junctions. *Phys. Rev. B* **100**, 024516 (2019).

[42] Kidwingira, F., Strand, J. D., Harlingen, D. J. V. & Maeno, Y. Parameter domains in Sr_2RuO_4. *Science* **314**, 1267–1271 (2006).

[43] Anwar, M. S. *et al.* Anomalous switching in $Nb/Ru/Sr_2RuO_4$ topological junctions by chiral domain wall motion. *Sci. Rep.* **3**, 2480 (2013).

[44] Mao, Z., Maeno, Y. & Fukazawa, H. Crystal growth of Sr_2RuO_4. *Mater. Res. Bull.* **35**, 1813–1824 (2000).

[45] Troeman, A. G. P. *et al.* Temperature dependence measurements of the supercurrent-phase relationship in niobium nanobridges. *Phys. Rev. B* **77**, 024509 (2008).

[46] Kumar, N., Fournier, T., Courtois, H., Winkelmann, C. B. & Gupta, A. K. Reversibility of superconducting nb weak links driven by the proximity effect in a quantum interference device. *Phys. Rev. Lett.* **114**, 157003 (2015).

[47] Michotte, S., Lucot, D. & Mailly, D. Fluxoid quantization in the critical current of a niobium superconducting loop far below the critical temperature. *Phys. Rev. B* **81**, 100503 (2010).

[48] Berdiyorov, G. R. *et al.* Large magnetoresistance oscillations in mesoscopic superconductors due to current-excited moving vortices. *Phys. Rev. Lett.* **109**, 057004 (2012).

[49] Cuevas, J. C. & Bergeret, F. S. Magnetic Interference Patterns and Vortices in Diffusive SNS Junctions. *Phys. Rev. Lett.* **99**, 217002 (2007).

[50] Chiodi, F. *et al.* Geometry-related magnetic interference patterns in long SNS Josephson junctions. *Phys. Rev. B* **86**, 064510 (2012).

[51] Blom, T. J. *et al.* Direct-write printing of Josephson junctions in a scanning electron microscope. *ACS Nano* **15**, 322–329 (2021).

[52] Bouhon, A. & Sigrist, M. Influence of the domain walls on the Josephson effect in Sr_2RuO_4. *New J. Phys.* **12**, 043031 (2010).

[53] Stoutimore, M. J. A. *et al.* Second-harmonic current-phase relation in Josephson junctions with ferromagnetic barriers. *Phys. Rev. Lett.* **121**, 177702 (2018).

[54] Yao, Y. *et al.* Half-integer shapiro steps in strong ferromagnetic Josephson junctions. *Phys. Rev. B* **104**, 104414 (2021).

[55] Willa, R., Hecker, M., Fernandes, R. M. & Schmalian, J. Inhomogeneous time-reversal symmetry breaking in Sr_2RuO_4. *Phys. Rev. B* **104**, 024511 (2021).

[56] Ramires, A. & Sigrist, M. Superconducting order parameter of Sr_2RuO_4: A microscopic perspective. *Phys. Rev. B* **100**, 104501 (2019).

[57] Suh, H. G. *et al.* Stabilizing even-parity chiral superconductivity in Sr_2RuO_4. *Phys. Rev. Research* **2**, 032023 (2020).

[58] Wu, J. *et al.* Electronic nematicity in Sr_2RuO_4. *Proc. Natl. Acad. Sci. U.S.A.* **117**, 10654–10659 (2020).

[59] Mao, Z. Q., Maeno, Y., NishiZaki, S., Akima, T. & Ishiguro, T. In-plane anisotropy of upper critical field in Sr_2RuO_4. *Phys. Rev. Lett.* **84**, 991–994 (2000).